





## RESEARCH ARTICLE OPEN ACCESS

# Fibroblasts and hiPS-Derived Astrocytes From CoPAN Patients Showed Different Levels of Iron Overload Correlated With Senescent Phenotype

Anna Cozzi<sup>1</sup> | Paolo Santambrogio<sup>1</sup>  | Andrea Stefano Moro<sup>2</sup> | Alessio Pelagatti<sup>1</sup>  | Alicia Rubio<sup>3,4</sup> | Chiara Balestrucci<sup>2</sup> | Ivano Di Meo<sup>5</sup>  | Valeria Tiranti<sup>5</sup> | Sonia Levi<sup>1,2</sup> 

<sup>1</sup>Division of Neuroscience, IRCCS San Raffaele Scientific Institute, Milan, Italy | <sup>2</sup>Vita-Salute San Raffaele University, Milan, Italy | <sup>3</sup>Institute of Neuroscience, National Research Council, Milan, Italy | <sup>4</sup>IFOM, Milan, Italy | <sup>5</sup>Unit of Medical Genetics and Neurogenetics, Fondazione IRCCS Istituto Neurologico Carlo Besta, Milan, Italy

**Correspondence:** Sonia Levi ([levi.sonia@hsr.it](mailto:levi.sonia@hsr.it))

**Received:** 13 January 2025 | **Revised:** 5 March 2025 | **Accepted:** 10 March 2025

**Funding:** This work was supported by Fondazione Telethon-Italy (Grants no. GGP11088, GGP16234, and GGP20047 to S.L.) and AISNAF (to S.L.).

**Keywords:** CoPAN disease | iron metabolism | mitochondrial dysfunction | NBIA disorders | neurodegenerative diseases

## ABSTRACT

COASY protein-associated neurodegeneration (CoPAN) is a rare autosomal recessive disorder within the Neurodegeneration with Brain Iron Accumulation spectrum, resulting from mutations in *COASY*. This gene encodes the bifunctional enzyme essential for the final steps of coenzyme A biosynthesis. To elucidate the pathophysiology and iron dyshomeostasis underlying CoPAN, we analyzed fibroblasts and human induced pluripotent stem (hiPS)-derived astrocytes from two patients carrying distinct *COASY* mutations. Our findings reveal that CoPAN fibroblasts display altered iron homeostasis, characterized by iron aggregates, elevated cytosolic labile iron pool, and impaired tubulin acetylation. Patients hiPS-derived astrocytes showed mitochondrial morphological abnormalities and compromised vesicular trafficking. Notably, both cell types demonstrated evidence of ferroptosis, but the astrocytes exhibited more pronounced iron accumulation and lipid peroxidation. These results demonstrate that astrocytes may more accurately recapitulate the pathological phenotype of CoPAN compared to fibroblasts. Interestingly, astrocytes exhibited different levels of iron accumulation concomitant with cellular senescence, indicating a possible role of iron-induced cellular senescence. This finding suggests that the accumulation of cytosolic iron, possibly caused by mitochondrial dysfunction, actively promotes senescence. Our data emphasize the potential therapeutic efficacy of drugs that enhance mitochondrial functionality to attenuate the effects of CoPAN.

## 1 | Introduction

COASY protein-associated neurodegeneration (CoPAN) (OMIM #615643) is a rare autosomal recessive disorder belonging to the family of Neurodegeneration with Brain Iron Accumulation (NBIA). It is caused by mutations in the *COASY* gene, located on chromosome 17q21, which encodes for the

bifunctional enzyme 4'-phosphopantetheine adenylyltransferase/dephospho-CoA kinase (PPAT/DPCK), also known as Coenzyme A (CoA) synthase (COASY). The onset of symptoms occurs in the first years of life and is mainly characterized by difficulties in movement and walking. As the disease progresses, dysarthria, oromandibular dystonia, paraparesis, bradykinesia, areflexia of the lower limbs and loss of the ability to

walk independently also occur. In addition, cognitive abilities are severely compromised and neuropsychiatric symptoms, such as obsessive-compulsive disorder and depression are present (Dusi et al. 2014). Patients' brain magnetic resonance images showed signs of hypointensity in the globus pallidus (GP) and bilateral hyperintensity and swelling in the caudate nucleus, putamen and thalamus. The "eye of the tiger" sign (Chang and Lin 2011), which is due to severe iron accumulation (Kruer et al. 2011), has also been found in some patients with CoPAN, but not in all (Evers et al. 2017). Increased levels of free carnitine, and decreased levels of acyl-carnitine, in the patients' blood were also detected (Evers et al. 2017).

The COASY enzyme, which consists of 564 amino acids, catalyzes the last two steps of CoA biosynthesis and is activated by the presence of phospholipids, such as phosphatidylcholine and phosphatidylethanolamine (Aghajanian and Worrall 2002). COASY has a mitochondrial localization, where it is present mainly in the matrix or associated with the outer membrane (Dusi et al. 2014). More recently, the presence of COASY has also been identified in the cytoplasm and nucleus (Lin et al. 2018). Analysis of fibroblasts obtained from CoPAN patients showed an alteration, but not a complete depletion, of CoA synthesis, thus suggesting a residual catalytic activity of the variant proteins or the presence of alternative pathways for the production and recycling of CoA (Dusi et al. 2014).

To date, 17 different COASY variants have been described (Ajit et al. 2023; Cavestro et al. 2024b; Dusi et al. 2014; Evers et al. 2017; Hashemi et al. 2023; Mahale et al. 2023; Rosati et al. 2023), which are associated with a wide range of clinical symptoms with some common features (Cavestro et al. 2024b; Dusi et al. 2014; Evers et al. 2017). Furthermore, complete loss of function mutations in COASY have also been associated with Pontocerebellar Hypoplasia (PCH) type 12, a rare neurodegenerative disorder characterized by hypoplasia of the cerebellum and pons. A characteristic feature of the pathology is the complete absence of COASY in the cells of affected patients, leading to a perinatally lethal phenotype. The search for iron aggregates in the brain, performed in a post-mortem patient, did not reveal accumulation of iron; this could be explained by the young age at the time of death (gestational age of 21 weeks) (Mishra et al. 2022; van Dijk et al. 2018). Variations in COASY have also recently been associated with a riboflavin-responsive lipid storage myopathy (RR-LSM) (Zheng et al. 2024). So far, a limited number of CoPAN models have been developed (Berti et al. 2015; Cavestro et al. 2024a; Di Meo et al. 2020; Khatri et al. 2016). In the yeast *Saccharomyces cerevisiae*, CoA synthesis involves a sequence of five enzymes (CAB1 to CAB5), and PPAT and DPCK activities reside on different proteins encoded by *CAB4* and *CAB5*, respectively (Berti et al. 2015). Deletion of both genes results in a lethal phenotype, which is rescued by the expression of the wild-type human COASY protein, while mutant COASY leads to severe consequences including pantothenate auxotrophy, reduced growth, decreased mitochondrial CoA levels, impaired mitochondrial respiratory chain, iron homeostasis dysfunction, and altered lipid content (Berti et al. 2015). When *coasy* is completely absent in zebrafish, it results in severe developmental abnormalities and early death. However, a partial reduction in *coasy* levels leads to milder phenotypes such as

reduced size, developmental defects in the nervous system, vascular arborization, and reduced embryonic CoA levels (Khatri et al. 2016). As COASY is an essential gene, the only mammalian model of COASY deficiency developed so far is conditional knockout mouse models, where *Coasy* is specifically deleted in neurons or in astroglial lineage (Cavestro et al. 2024a; Di Meo et al. 2020). Both models exhibit severe early-onset neurological impairment, characterized by growth arrest, locomotor abnormalities, and dystonia. Post-mortem analysis of the brains of these mice revealed alterations in mitochondrial structure and/or function, as well as changes in iron homeostasis, including increased Ferritin-L, the cytosolic iron storage protein, and decreased transferrin receptor 1 (TfR1) and divalent metal transporter 1, two of the iron cellular importers (Cavestro et al. 2024a; Di Meo et al. 2020). Interestingly, the astroglial conditional model showed a severe cortical and cerebellar hypoplasia, suggesting a critical role of *Coasy* also in neurodevelopment (Cavestro et al. 2024a). The relationship between iron dys-homeostasis and CoA deficiency has been studied more thoroughly in disease models of PKAN (Arber et al. 2017; Orellana et al. 2016), a pathology associated with alteration of PANK2, the enzyme that catalyzes the first reaction of the CoA pathway (Hayflick 2023; Leonardi et al. 2005). In particular, the studies on hiPS-derived astrocytes highlighted the pathogenic mechanism that leads to cytosolic iron accumulation. Briefly, CoA restriction alters tubulin acetylation (Santambrogio et al. 2024), which impairs normal TfR1 endocytosis (Ripamonti et al. 2022), reducing iron transport to the mitochondrion (Santambrogio et al. 2024). The cell compensates for mitochondrial iron deficiency by a continuous recall of iron which is not properly distributed intracellularly and accumulates in the cytosol (Santambrogio et al. 2024). Here, using human fibroblasts and hiPS-derived astrocytes as disease models, we found that also COASY variants are associated with altered tubulin acetylation and variable cellular iron accumulation. This variation depends on the cell type and the specific gene mutations and correlates with different degrees of cellular senescence. Moreover, d-astrocytes from both patients showed signs of ferroptosis, an iron-dependent regulated form of cell death.

## 2 | Methods

All methods have related literature references. All fibroblasts and d-astrocytes from controls and CoPAN patients were subjected to the same analyses, with one example reported in each figure. Further protocol information is available from the corresponding author upon reasonable request.

Primary fibroblast cell lines were generated from skin biopsies from two patients obtained from the Movement Disorders Bio-Bank available at Fondazione IRCCS Istituto Neurologico Carlo Besta and two healthy subjects purchased from ATCC.

### 2.1 | Cell Models

The fibroblasts were cultured in high glucose Dulbecco's Modified Eagle Medium with or without the addition of 15  $\mu$ M FAC, 1  $\mu$ M Apo-Tf, 200  $\mu$ M Ascorbic acid supplemented with

10% fetal bovine serum from two different batches (named A or B) (Euroclone, Pero, Italy) 1% penicillin/streptomycin, and 2 mM L-glutamine (Sigma-Aldrich, Milano, Italy), at 37°C in a 5% CO<sub>2</sub> humidified atmosphere (Dusi et al. 2014). In the experiments the type of serum was not specified is intended the use of serum A without addition of iron. We reprogrammed fibroblasts from two CoPAN patients and two normal subjects (controls) via Sendai virus-mediated expression of the four Yamanaka's factors to obtain CoPAN and control transgene-free hiPS clones (Orellana et al. 2016; Takahashi and Yamanaka 2006). Independent hiPS clones for each of the two CoPAN patients and the two controls were generated and fully characterized.

COASY gene was amplified by PCR using genomic DNA as a template. The primers used were (5'-3'): c.C175T-Fw-GTCTCCTG GTGCTGACGAC, c.C175T-Re-CCTACCCTTCCTTGATCTCG, c.C1495T-Fw-GAGGATGGCAACAGCTAAGG, c.C1495T-Re-AACCAGGTGAGCATCAAG. The PCR products were inserted into a shuttle vector (TOPO TA cloning kit, Thermo Fisher) and then Sanger sequencing was performed.

The same hiPS clones for each control and CoPAN patients were differentiated into a pure and stable population of mature astrocytes as in (Santambrogio et al. 2022). Briefly, NPCs were seeded onto iMatrix-511 (Amsbio, Cambridge, MA, USA)-coated plates and grown in DMEM-F12 (Euroclone) supplemented with 1% Pen/Strep (Sigma-Aldrich), 2 mM L-glutamine (Sigma-Aldrich), N2 (1:100; Life Technologies), B27 (1:200; Life Technologies, Carlsbad, CA, USA), and bFGF (20 ng/mL; Tebu-Bio, Magenta, Italy). When the cell culture reached a confluence of approximately 60%, the medium was supplemented with 20% FBS (Euroclone), and the medium was changed every 2–3 days. The culture was maintained for more than 40 days to produce astrocytes with a good level of maturation.

## 2.2 | Cell Viability Assay

A total of  $2 \times 10^4$  cells were plated in 96-well plates, grown for 18 h at 37°C in medium, and then incubated with 10  $\mu$ L MTT solution (5 mg/mL in phosphate-buffered saline 1X) for 2 h at 37°C. The color absorbance was read at 570 nm following the manufacturer's instructions (Sigma-Aldrich) (Cozzi et al. 2019).

## 2.3 | Immunofluorescence and Immunoblotting

Cells grown on coverslips were fixed in 4% paraformaldehyde and processed for immunofluorescence as described in (Santambrogio et al. 2020). Specific antibodies and conditions are listed in Table S1. Images were acquired by a Zeiss Axio Observer Z1 fluorescence microscope equipped with a Hamamatsu FM-CCD 9100-02 camera and Volocity acquisition software. Immunoblotting was performed after separation of soluble proteins (25  $\mu$ g) by SDS-PAGE as in (Orellana et al. 2016) treated or not with different reagents (100  $\mu$ M Ferrum Ammonium Citrate and 200  $\mu$ M Ascorbic Acid, 100  $\mu$ M Deferiprone, 25  $\mu$ M CoA 10 nM Min102) at the time indicated. Specific antibodies and conditions are listed

in Table S1. The signal was revealed using an ECL Prime Kit (Merck, Rome, Italy) and detected with a ChemiDoc MP Imaging System (BIORAD, Segrate, Italy). Total protein contents were measured using the BCA Protein assay (Thermo Fisher Scientific, Monza, Italy) calibrated with Bovine Serum Albumin.

## 2.4 | Perls Staining

Fibroblasts and d-astrocytes from CoPAN patients and controls, grown on coverslips for 72 h, were fixed in 4% paraformaldehyde and were stained for iron content via the Perls reaction, incubating them for 1 h in 1% potassium ferrocyanide (K<sub>4</sub>[Fe(CN)<sub>6</sub>] • 3H<sub>2</sub>O) and 1% hydrochloric acid in distilled water. Cells were counterstained with Nuclear Fast Red (Sigma-Aldrich). Images were taken on a Zeiss AxioImager M2m equipped with AxioCam MRc5 using a 40 $\times$  objective.

## 2.5 | Determination of Cytosolic LIP

Cytosolic LIP was measured in fibroblasts incubated for 24 h in a 96-well plate, using the iron-sensitive fluorescent probe calcein (Thermo Fisher Scientific), as described in (Santambrogio et al. 2024). Basal fluorescence was acquired using an Arrayscan XTI HCA Reader (Thermo Fisher Scientific) equipped with an LD Plan-NEOFLUAR 20 $\times$ /0.4NA objective (Zeiss, Milan, Italy). Excitation LED (386/23 nm) was used for Hoechst, LED (485/20 nm) was used for calcein, and a pentaband BGRFRN dichroic mirror and emission filter were used for both. Total calcein fluorescence was measured after the release of iron bound to the probes by the addition of the specific iron chelator PIH (1 mM) for 30 min. The difference between total and basal fluorescence represents the cytosolic LIP. The results were normalized using Hoechst fluorescence as an estimation of the number of cells.

## 2.6 | H-Ferritin Quantification

H-Ferritin level was determined by ELISA assay using the monoclonal antibody rH02 (homemade) calibrated on the corresponding recombinant homopolymer (Cozzi et al. 1989).

## 2.7 | Electron Microscopy

CoPAN patients and controls d-astrocytes were fixed in 4% paraformaldehyde and 2.5% glutaraldehyde, post-fixed with 2% OsO<sub>4</sub>, washed, dehydrated, and embedded in Epon812. Thin sections were stained with uranyl acetate and lead citrate and examined in a Leo912 electron microscope (Zeiss). Images were randomly obtained under blind conditions to the examiner.

## 2.8 | SA- $\beta$ -Gal Activity Detection

The cells were analyzed according to the protocol "Senescence Cells Histochemical Staining" (Sigma-Aldrich). This assay is based on a histochemical stain for  $\beta$ -galactosidase activity

at pH6. In brief, the cells were fixed with a solution containing 20% formaldehyde and 2% glutaraldehyde, stained with a solution of X-gal, and incubated at 37°C for 18h. The cells were observed under bright light: the blue-stained cells and total number of cells were counted, and the percentage of cells expressing  $\beta$ -galactosidase was calculated.

## 2.9 | SynaptoZip and Synbond Uptake

Lentiviral vectors encoding SynaptoZip (SZ) were prepared and used as described in (Ferro et al. 2017) to infect astrocytes at 30 days of age. Experiments using fluorescent Synbond (SB) were performed on astrocytes between 60 and 80 days old. Cells expressing SZ were incubated live with 5 nM SB-Alexa-568 for either 5 or 30 min at 37°C and 5% CO<sub>2</sub> in serum-free DMEM F12. After incubation, the cells were washed with PBS at 4°C supplemented with 1% BSA, rinsed with cold PBS, fixed with 4% paraformaldehyde, and analyzed for retrospective fluorescence analysis. Fluorescence was acquired via confocal imaging using a LEICA TCS SP5 laser scanning microscope (Wetzlar, Germany), equipped with the appropriate emission/absorption filters. Laser parameters were set to avoid pixel saturation, and images were captured at a resolution of 2048×2048, 12-bit, with either a 40×/1.25 NA or 63×/1.4 NA oil objective for analysis. The mean fluorescence of individual vesicles was calculated for each image, and vesicle segmentation was performed semi-automatically on the SZ signal using MATLAB (Mathworks, Natick, United States) standard built-in functions/plugins, as previously described (Ripamonti et al. 2022).

## 2.10 | Statistical Analyses

No statistical methods were employed to predetermine the sample size in the experiments. Normally distributed data were analyzed using a two-tailed unpaired Student's *t*-test or one-way ANOVA followed by the Holm-Sidak post-test in GraphPad Prism (version 6.0). The SynaptoZip experiments were analyzed using a two-way ANOVA followed by a post hoc Holm test using R (version 4.4.1). Data are reported as means ± SD or SEM. A *p*-value < 0.05 was considered statistically significant.

Multiple LMEs were fitted to the data, with different fixed and random effect factors as described in the Results section. ANOVA or Kenward-Roger tests were performed on the fitted models. The normality of the dependent variable distributions, as well as the residuals of the LME models, was assessed graphically using qqplots and histograms. For correlation analyses, Pearson's correlation coefficient was used. These analyses were conducted using R (version 4.4.1).

Two formulas for each of the four western-blot targets (GPX4, MDA, 4HNE, and NCOA4) were fitted using the following formulas (Wilkinson notation):

$$Y \sim 1 + \text{CoPAN} + \text{Cell Type} + \text{CoPAN} \cdot \text{Cell Type} + (1 | \text{subject}) + (1 | \text{experiment}) \quad (1)$$

and

$$Y \sim 1 + \text{CoPAN} + \text{Cell Type} + (1 | \text{subject}) + (1 | \text{experiment}) \quad (2)$$

Where *Y* represents the normalized values obtained from the Western Blot (the ratio between the protein and the house-keeping gene, all normalized to a control) for GPX4, MDA, 4HNE, and NCOA4. Among the fixed effect factors evaluated, CoPAN indicates whether the measurement is from a patient or a control, Cell Type indicates the type of cell, either fibroblast or astrocyte, while CoPAN · Cell Type is the interaction between these two variables. Finally, two random effects, one for the subject and the other for the experimental session, were added.

## 3 | Results

### 3.1 | Characterization of CoPAN Fibroblasts Highlighted Alteration of Iron Homeostasis

We analyzed fibroblasts originating from two CoPAN patients (Dusi et al. 2014). The first one is a compound heterozygous for two variants: the c.175C>T transition, causing the p.Gln59\* variation, which leads to the appearance of a premature STOP codon in the regulatory region present at the N-terminus of the protein (Dusi et al. 2014) (Figure S1A); and the c.1495C>T transition, which causes the p.Arg499Cys missense change in the amino acid sequence (here named CoPAN<sub>[Arg499Cys+Gln59\*]</sub>). This latter alteration hits the DPCK domain of the protein and affects a highly conserved amino acid residue (Figure S1A), essential for the binding between the protein and ATP, as well as for the transfer of the phosphate group (Dusi et al. 2014). The second patient carries the c.1495C>T variant in both alleles, leading to homozygous p.Arg499Cys (Figure S1A) (here named CoPAN<sub>[Arg499Cys]</sub>) (Dusi et al. 2014). They were investigated in parallel with two controls derived from healthy subjects (see Materials and methods).

The MTT assay demonstrated a reduced viability of both CoPAN fibroblasts compared to controls (Figure S1B), suggesting a compromised physiological function. Immunoblotting analysis conducted on fibroblast lysates indicated the absence of the COASY protein in the CoPAN<sub>[Arg499Cys+Gln59\*]</sub> and a detectable protein level in CoPAN<sub>[Arg499Cys]</sub> (Figure S1C).

By a bioinformatic tool (SIREs program, <http://ccbg.imppc.org/sires/>), Arber and coworkers (Arber et al. 2016) previously identified the presence of a hypothetical Iron Responsible Element (IRE) in the 3' UTR region of the COASY transcript (Figure S1A). The canonical IRE sequence is recognized by IRP1/2 proteins (Hentze et al. 2010), the iron sensor proteins that, based on cellular iron concentration, regulate the translation of proteins involved in maintaining iron homeostasis. Thus, the presence of a functional IRE sequence on the COASY transcript could be utilized to modulate the amount of protein by variation of iron concentration to increase the protein level. The functionality of the IRE sequence was tested upon cell treatment with iron addition (100 μM Ferric ammonium Citrate, FAC) or with an iron chelator (100 μM Deferiprone, DFP) for 18h. The results showed that the level of COASY



protein did not change after the treatments (Figure S1C), indicating that COASY is not modulated by iron concentration.

However, the investigation of cellular iron metabolism revealed the alteration of iron parameters in CoPAN fibroblasts, with respect to the control cells (Figure 1). Either the presence of Perls positive iron aggregates, indicative of iron accumulation (Figure 1A), and the increase of the cytosolic

labile iron pool (Figure 1B) suggested the alteration of iron concentration in CoPAN fibroblasts, which is confirmed by the increased amount of the iron storage protein Ferritin-H (FtH) (Figure 1C) and by the decrease of the iron importer Transferrin Receptor (TfR1) (Figure 1D). However, both Ferroportin (Fpn) (Figure S2A) and Divalent Metal Transporter 1 (DMT1-IRE) are not expressed significantly differently (Figure S2B).

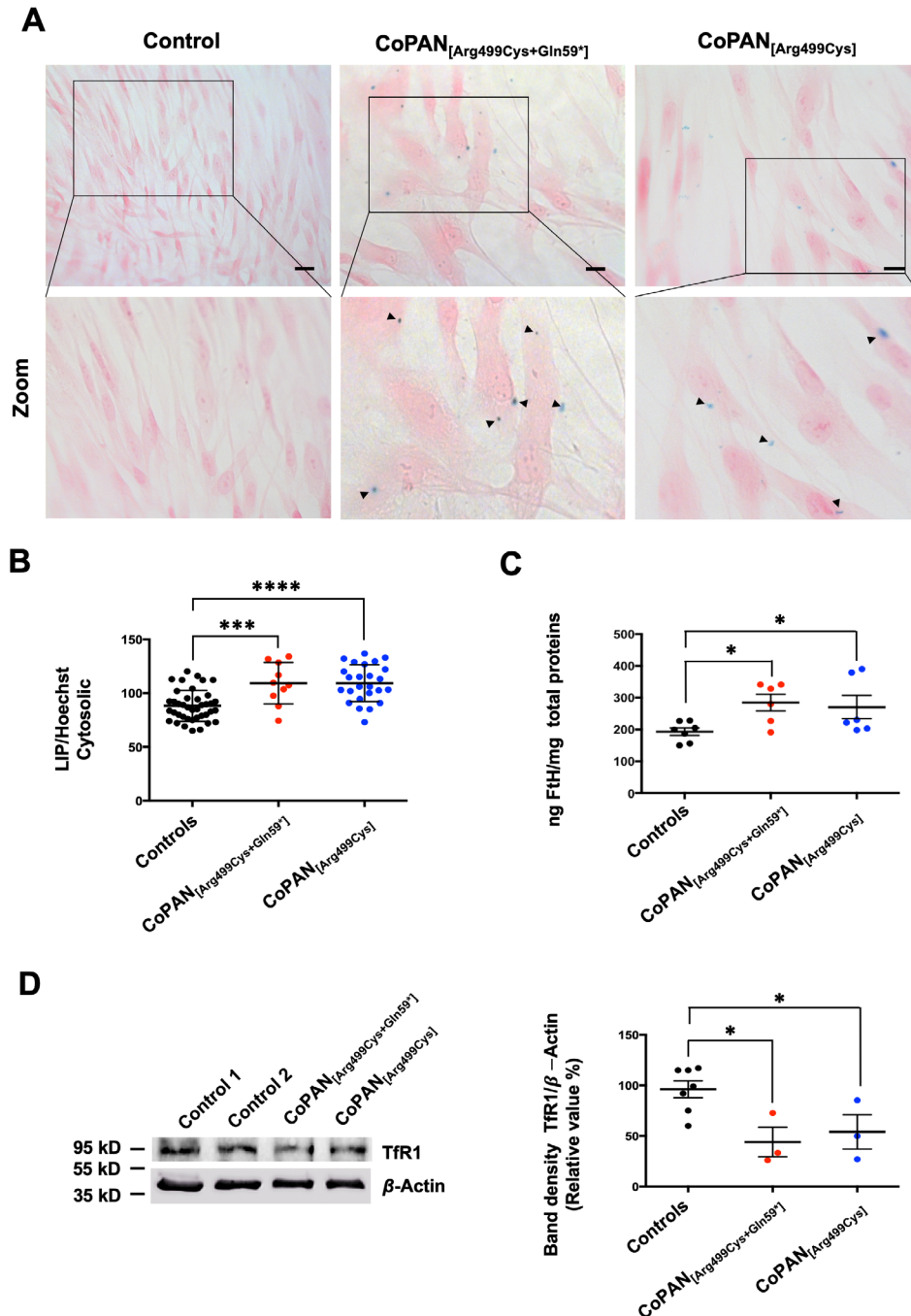


**FIGURE 1** | Cellular iron mobilization in CoPAN fibroblasts. (A) Representative image of fibroblasts from control and CoPAN patients stained with the iron-specific Perls reaction (blue), and counterstained with nuclear fast red. The arrowheads show the iron aggregates. Scale bars 20 μm (B) Evaluation of cytosolic Labile Iron Pool (LIP) in fibroblasts stained with specific probe calcein and Hoescht. The graph shows the mean ± SEM of three independent experiments (one-way ANOVA). (C) H-Ferritin chain (FtH) level determined by ELISA assay on soluble cell homogenates from fibroblasts. The graph shows the mean ± SEM of three independent experiments (one-way ANOVA). (D) Western blot of soluble cell homogenates from fibroblasts probed with the indicated antibody. Quantification of TfR1 protein normalized to Actin by densitometry. The graph shows the mean ± SEM of three independent experiments (one-way ANOVA) (right panel). \* $p < 0.05$ , \*\*\* $p < 0.001$ , \*\*\*\* $p < 0.0001$ .

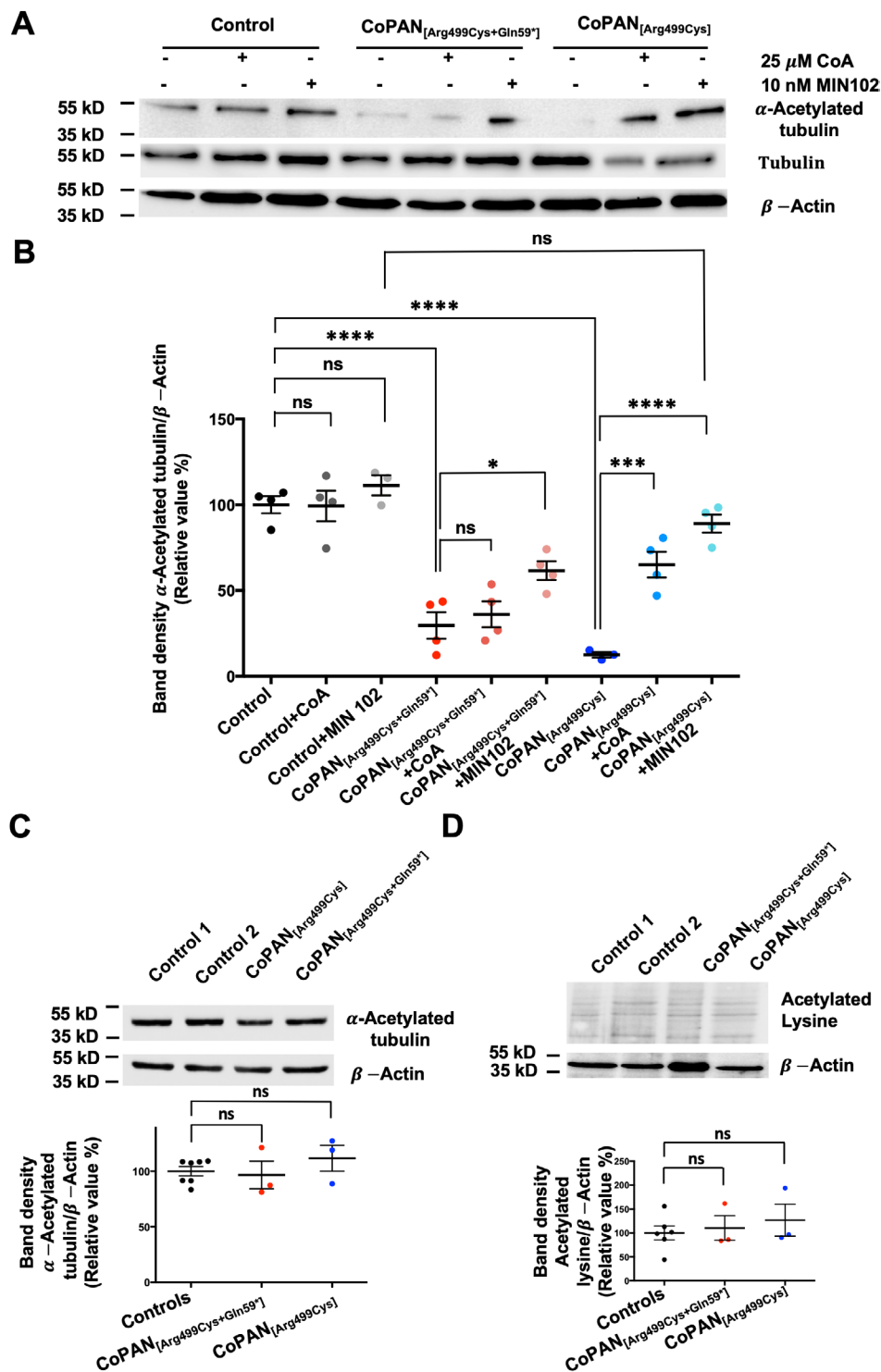


**FIGURE 2** | Acetylation in CoPAN fibroblasts. (A) Western blot of soluble cell homogenates from control and CoPAN patients' fibroblasts (grown in supplemented serum B), in the presence or absence of 25  $\mu$ M CoA or 10 nM MIN102, probed with the indicated antibody. (B) Quantification of the proteins normalized to Actin by densitometry. Graph indicates the means  $\pm$  SEM of three independent experiments (one-way ANOVA). (C) Western blot of soluble cell homogenates from control and CoPAN patients' fibroblasts probed with the indicated antibody (above), quantification of the  $\alpha$ -acetylated tubulin normalized to Actin by densitometry when fibroblasts are grown in non-supplemented serum (below). Graph indicates the mean  $\pm$  SEM of three independent experiments (one-way ANOVA). (D) Western blot of soluble cell homogenates from control and CoPAN patients' fibroblasts probed with the indicated antibody (above), quantification of the Acetylated lysine normalized to Actin by densitometry (below). Graph indicates the means  $\pm$  SEM of three independent experiments (one-way ANOVA). \* $p$  < 0.05, \*\*\* $p$  < 0.001, \*\*\*\* $p$  < 0.0001.

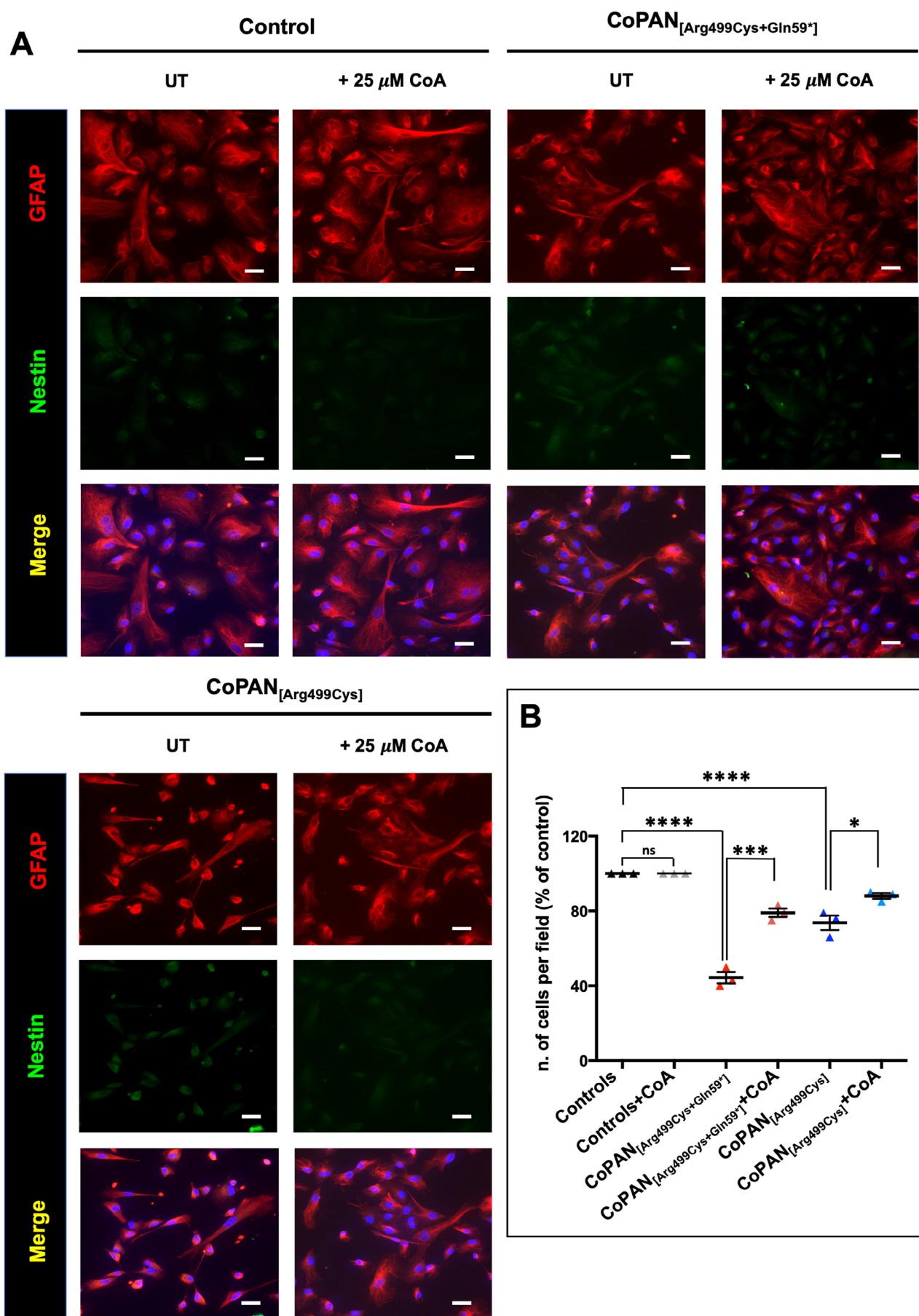


FIGURE 3 | Legend on next page.

**FIGURE 3** | Characterization and cell viability of d-astrocytes. (A) Representative immunofluorescence images of d-astrocytes from control and CoPAN patients differentiated for 40 days in the presence or absence of 25  $\mu$ M CoA. Astrocytes were stained with the specific marker glial fibrillary acidic protein (GFAP) and with Nestin to detect the possible presence of neural stem cells. Nuclei were stained with Hoechst. Scale bars 20  $\mu$ m. (B) The graph shows the GFAP positive d-astrocytes, plotted as the percentage with respect to the controls of the total cells in 10 fields from three independent experiments. Means  $\pm$  SD (one-way ANOVA) \* $p$  < 0.05, \*\*\* $p$  < 0.001, \*\*\*\* $p$  < 0.0001.

### 3.2 | CoPAN Fibroblasts Showed Altered Tubulin Acetylation

One of the effects of CoA restriction is the alteration of protein acetylation (Galdieri et al. 2014; Siudeja et al. 2011). In our previous study (Santambrogio et al. 2024), the alteration of tubulin acetylation was identified as responsible for the mechanism underlying the accumulation of cytosolic iron in PKAN disease. To verify whether this alteration also occurs in CoPAN cells, we tested the level of  $\alpha$ -acetylated tubulin that resulted in a strongly decreased level in CoPAN fibroblasts compared to the control (Figure 2A,B).

We observed that tubulin acetylation strongly depended on the presence of iron in the medium. It occurred that the use of serum B alone or added to iron (see Materials and Methods) correlated with Perls negativity or positivity in patient fibroblasts. In fact, by supplementing the medium prepared with serum B with physiological concentrations of transferrin and iron (by adding 1  $\mu$ M Apo-Tf, 15  $\mu$ M Ferric ammonium Cytrate (FAC), and 200  $\mu$ M Ascorbic acid to make iron available to Tf), we noticed that Perls positivity was restored in patient fibroblasts, leaving the controls unaltered.

Interestingly, when we used the non-supplemented medium with serum B, we observed no difference in  $\alpha$ -acetylated tubulin (Figure 2C) as well as in Perls positivity (data not shown), further corroborating the crucial role of iron in determining this phenotype.

In addition, the levels of acetylated tubulin can be restored to varying degrees (Figure 2A,B) by treating the cells with CoA and, more effectively, with leriglitazone (5-[[4-[2-[5-(1-hydroxyethyl)pyridine-2-yl]ethoxy] phenyl]methyl]-1,3-thiazolidine-2,4-dionehydrochloride), a peroxisome proliferator-activated receptor gamma agonist (here named MIN-102), previously proven effective in PKAN (Santambrogio et al. 2023), that at least for one patient restored the acetylation level to the same extent as control (Figure 2A,B).

We also tested the total lysine acetylation of cell homogenates by immunoblotting. This analysis did not reveal a statistically significant difference between CoPAN and control cells (Figure 2D).

### 3.3 | CoPAN Astrocytes Show Mitochondrial Morphology and Vesicular Trafficking Impairments

To obtain a model that better recapitulates the disease, we reprogrammed these CoPAN and control fibroblasts into transgene-free hiPS clones (see Materials and Methods) (Orellana et al. 2016; Takahashi and Yamanaka 2006). We selected one clone for each

of the two CoPAN patients and the two controls. The preservation of the patients' mutations was confirmed by Sanger sequencing on the newly obtained hiPS clones (Figure S3A) and the correct karyotype was regularly tested (not shown). The expression of master regulators of pluripotent stem cells and associated markers, Nanog, Tra1-60, Oct4, and Sox2, was assessed by immunofluorescence analysis, and the results confirmed the stem cell pluripotency state of the hiPS lines (Figure S3B). Control and CoPAN hiPS clones were differentiated into neuronal precursor cells (NPCs) (Orellana et al. 2016), and then into astrocytes (d-astrocytes) (Santambrogio et al. 2022; Santambrogio et al. 2024). Nearly all the cells were positive for the astrocyte-specific marker GFAP, while negative for Nestin, a marker of neural stem cells (Figure 3A), as well as positive for the astrocytic EAAT2 and negative for the neuronal Map2 markers (not shown), demonstrating that these cultures were virtually composed of astrocytes. Moreover, the development of d-astrocytes in the presence of 25  $\mu$ M CoA did not influence the quality of the final product (Figure 3A), while it ameliorated the reduced viability of the mutated d-astrocytes (Figure 3B). Ultrastructural analysis of d-astrocytes revealed the presence of morphological alterations of mitochondria in CoPAN specimens; they appeared abnormal, enlarged, and swollen with damaged cristae (Figure 4A). By measuring the larger diameter perpendicular to the longitudinal axis of more than 40 mitochondria per subject, a difference in the distribution of diameter lengths was revealed, implying a higher proportion of altered mitochondria in CoPAN compared to control d-astrocytes (Figure 4B).

To verify if the CoA impairment affects vesicular trafficking, as we have previously revealed in PKAN (Ripamonti et al. 2022), we used the activity-enriching biosensor SynaptoZip tool (Ferro et al. 2017). This tool utilizes an engineered VAMP2 protein that binds to a small fluorescent peptide, Synbond (SB), within the vesicle lumen. By expressing this protein, termed SynaptoZip, individual vesicles undergoing exo-endocytosis can be irreversibly tagged, allowing for the quantification of individual endosome activity based on the cumulative fluorescence of Synbond-enriched vesicles. The analysis of this dynamic indicated different behavior among the two patients. Specifically, at both time points, CoPAN<sub>[Arg499Cys+Gln59\*]</sub> showed a marked reduction of SB uptake with respect to the control, while CoPAN<sub>[Arg499Cys]</sub> seemed to uptake slightly more SB, especially at 5 min (Figure 4C,D).

### 3.4 | CoPAN Astrocytes Accumulated a Huge Amount of Iron

Iron deposition was tested on d-astrocytes after 40–50 days in vitro (DIV) by the specific Perls reaction that showed about 80% and 35% iron-positive cells in CoPAN<sub>[Arg499Cys+Gln59\*]</sub> and CoPAN<sub>[Arg499Cys]</sub>, respectively, while only 3% of the control cells



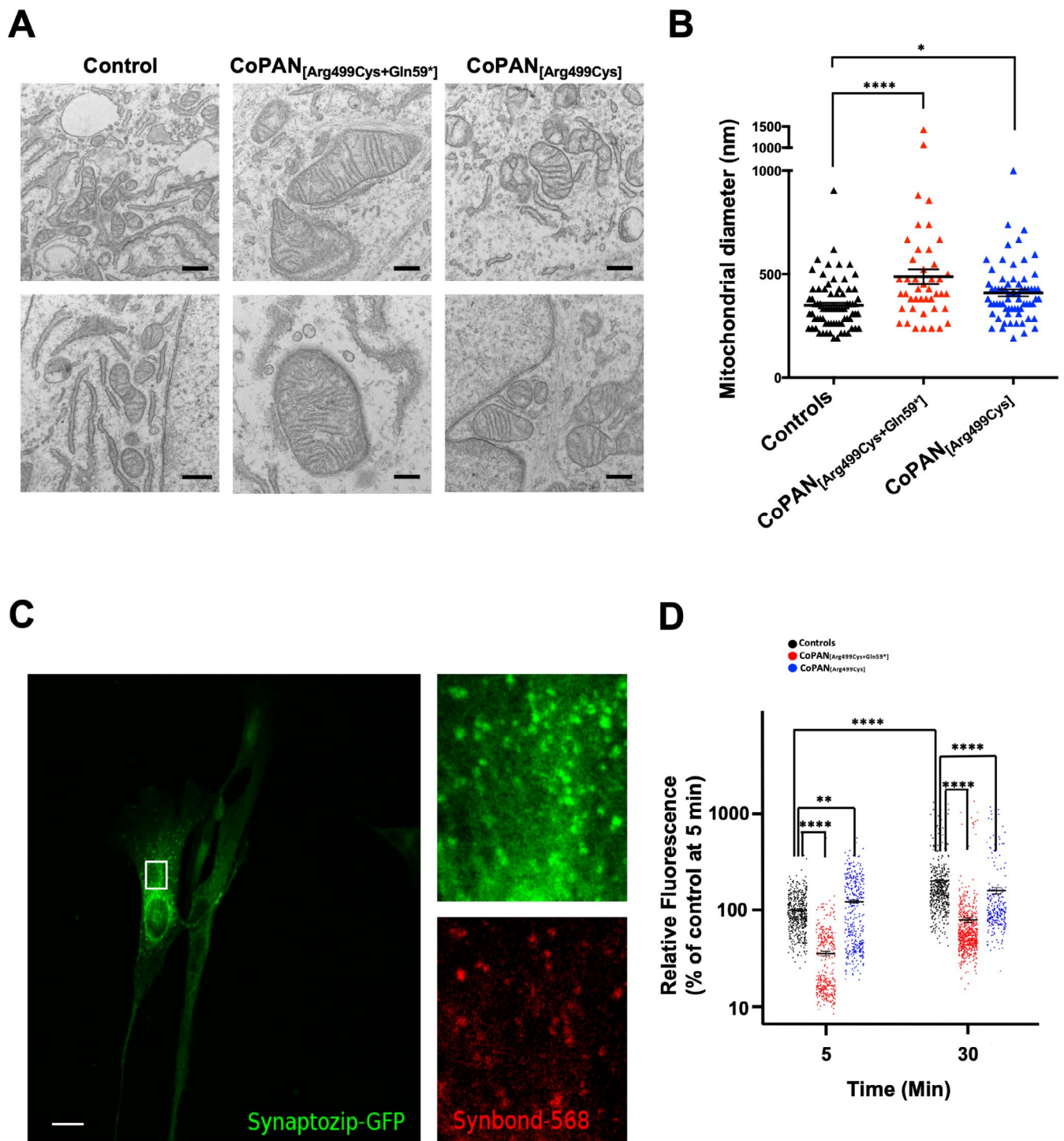


**FIGURE 4** | Affected mitochondrial morphology and vesicular trafficking in CoPAN human d-astrocytes. (A) Representative image of ultrastructural analysis of fixed d-astrocytes examined under an electron microscope. Scale bar 500nm. (B) Mitochondrial size was measured at the level of the larger diameter along the perpendicular axis in more than 40 mitochondria for each sample. Graphic shows the mitochondrial diameter. Means  $\pm$  SD (one-way ANOVA). (C) Representative image of immunofluorescence of fixed d-astrocytes examined by confocal microscopy. In green is the expression of SynaptoZip, and in red, its SynBond uptake. Scale bar 20 $\mu$ m. (D) The graph displays the mean fluorescence of SB, in tagged vesicles, expressed in percentage relative to control at 5 min. The black dots represent the control samples, while CoPAN<sub>[Arg499Cys+Gln59\*]</sub> is shown in red and CoPAN<sub>[Arg499Cys]</sub> in blue. Means  $\pm$  SD, (two-way ANOVA) \* $p$  < 0.05, \*\* $p$  < 0.01, \*\*\*\* $p$  < 0.0001.

were slightly positive (Figure 5A,B). Furthermore, d-astrocytes were also differentiated in the presence of 25 $\mu$ M CoA, and the percentage of Perls-positive cells was significantly reduced in both patients (Figure 5A,B). Similarly to fibroblasts, TfR1 showed a decrease in patients compared to controls (Figure 5C).

### 3.5 | CoPAN Astrocytes Showed a Variable Senescent Phenotype

Ultrastructural analysis, revealed not only the alteration of mitochondrial morphology, but also the presence of

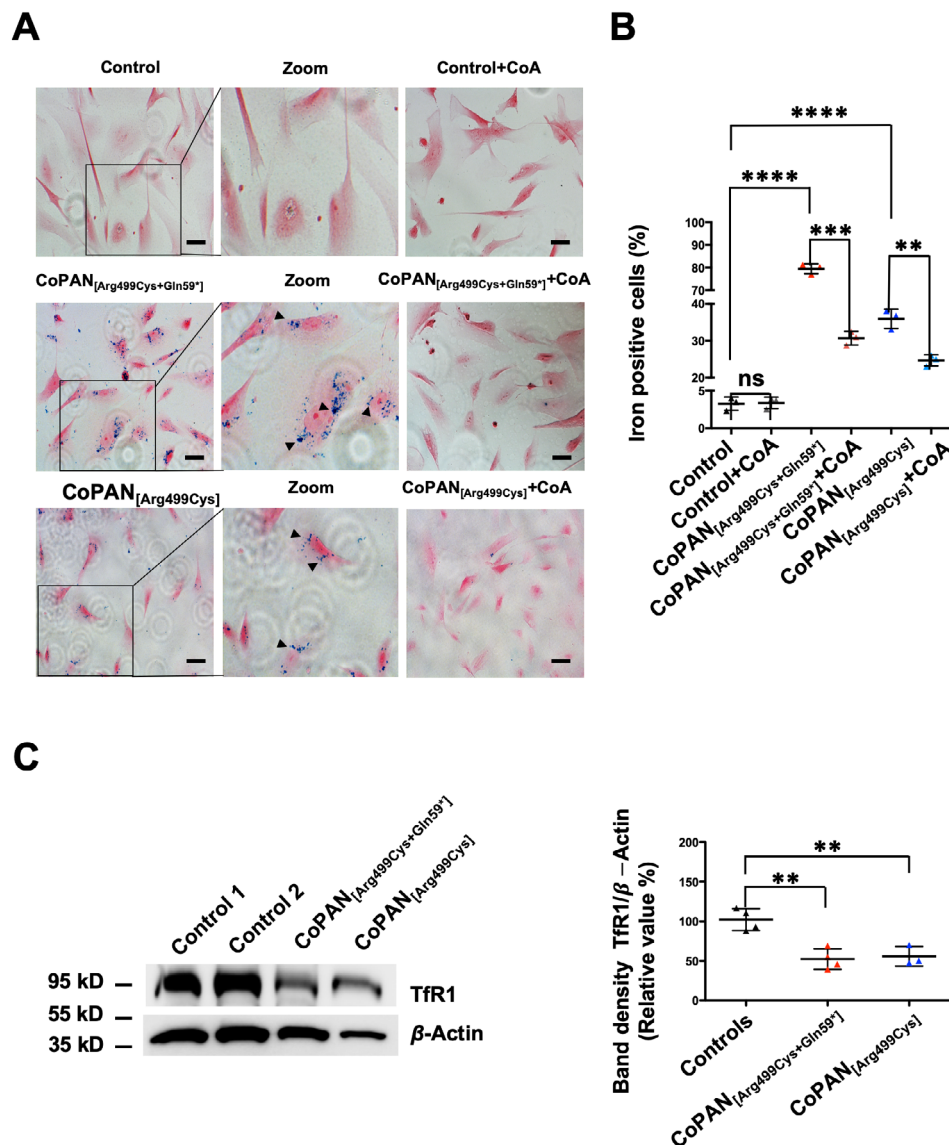


**FIGURE 5** | Iron accumulation in d-astrocytes. (A) Representative image of d-astrocytes from control and CoPAN patients, differentiated for 50 days in the presence or absence of 25  $\mu$ M CoA, stained with the iron-specific Perls reaction (blue) and counterstained with nuclear fast red. Scale bars 20  $\mu$ m. (B) Graphic showing the percentage of cells positive for iron staining. Means  $\pm$  SD of three independent experiments (one-way ANOVA). (C) Western blot of soluble cell homogenates from fibroblasts probed with the indicated antibody. Quantification of TfR1 protein normalized to Actin by densitometry. The graph shows the mean  $\pm$  SEM of three independent experiments (one-way ANOVA) (right panel) \*\* $p$  < 0.01, \*\*\* $p$  < 0.001, \*\*\*\* $p$  < 0.0001.

vacuolar structures (Figure 6A) reminiscent of senescent cells (Cozzi et al. 2019; Malatesta et al. 2011), particularly in CoPAN<sub>[Arg499Cys+Gln59\*]</sub>. To verify cellular senescent phenotype, we tested the  $\beta$ -Galactosidase activity, a biomarker of senescence. This analysis performed on d-astrocytes indicated about 80% of positive cells in CoPAN<sub>[Arg499Cys+Gln59\*]</sub> and around 2% of positive cells in CoPAN<sub>[Arg499Cys]</sub> (Figure 6B,C), comparable to the control, while the  $\beta$ -Galactosidase activity evaluated on fibroblasts showed around 1% of positive cells either in patients and controls (not shown). These data were evocative of the results obtained by Perls analysis (Figures 1A and 5A), suggesting a relationship between iron deposition and senescence. To correlate these two features, we plot the mean % of  $\beta$ -Gal positive cells versus the mean % of Perls positive cells using experiments done on both astrocytes and

fibroblasts. The analysis showed a high correlation ( $=0.928$ ) between these two factors (Figure 6D).

### 3.6 | Only CoPAN Astrocytes Showed a Tendency to Lipid Peroxidation and Ferroptosis

The apparent difference in iron accumulation in the two cellular models prompted us to consider further whether there are other distinct pathological phenotypes that could be emphasized, taking into account all possible variables: the effect of disease (patients versus controls) and/or an interaction between cell type (fibroblasts and d-astrocytes) and disease (controls and patients). All the following experiments were conducted by culturing fibroblasts and astrocytes in medium

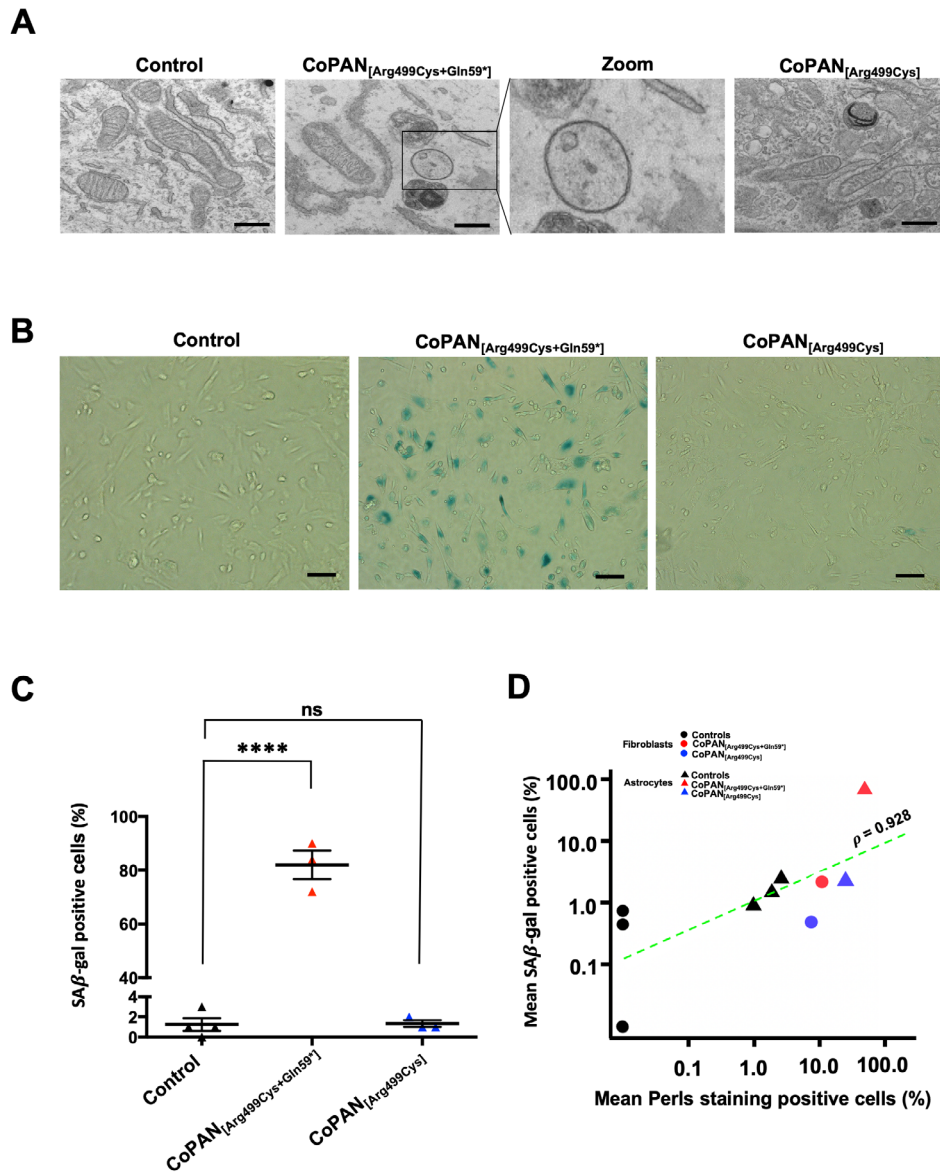


**FIGURE 6** | Iron-induced senescence in d-astrocytes. (A) Representative image of ultrastructural analysis of fixed examined with an electron microscope. Scale bar 500 nm. (B) Representative image of SA-gal activity in controls and CoPAN patients d-astrocytes (bright field). Scale bars 20  $\mu$ m. (C) Positively stained cells were counted and plotted as the percentage of the total cells ( $n = 100$  cells). The results are presented as the mean  $\pm$  SD in three independent experiments (one-way ANOVA). (D) The scatter plot shows CoPAN patients' fibroblasts (blue and red circles) and d-astrocytes (blue and red triangles), while the corresponding black symbols identify the controls. A Pearson correlation coefficient ( $\rho = 0.928$ ) indicates a strong positive correlation between the number of  $\beta$ -gal-positive cells and the number of Perls-positive cells. \*\*\* $p < 0.0001$ .

containing serum B and supplemented with Apo-Tf, FAC, and ascorbic acid.

We used LME analysis (see Materials and Methods) to evaluate by immunoblotting experiments the expression of markers of ferroptosis (Glutathione peroxidase, GPX4, and Nuclear Receptor Coactivator 4, NCOA4) and the presence of lipid peroxidation (malondialdehyde, MDA, and 4-hydroxy-2-nonenal, 4HNE) (Doll and Conrad 2017). GPX4 is an antioxidant enzyme that controls lipid peroxidation, reducing it in its hydroxyl form (Ursini and Maiorino 2020). Another parameter involved in iron management and ferroptosis is NCOA4, a selective cargo receptor that mediates the autophagic degradation of ferritin and is involved in DNA replication and in many other metabolic

pathways (Le et al. 2024); while MDA and 4HNE are the products of lipid peroxidation (Ayala et al. 2014).

GPX4 expression is decreased, and the level of MDA is elevated only in d-astrocytes, distinguishing patients from controls (Figure 7A,B), as expected in ferroptotic cells.

Regarding 4HNE, we found the same behavior in the two types of cells without a significant difference in patients and controls (Figure 7C). Evaluation of NCOA4 on cellular homogenates resulted in a decrease in CoPAN subjects independently of cell types (Figure 7D). Therefore, it is likely that the decrease in NCOA4 depends exclusively on having a *COASY* mutation and, considering that both cell types showed iron accumulation,



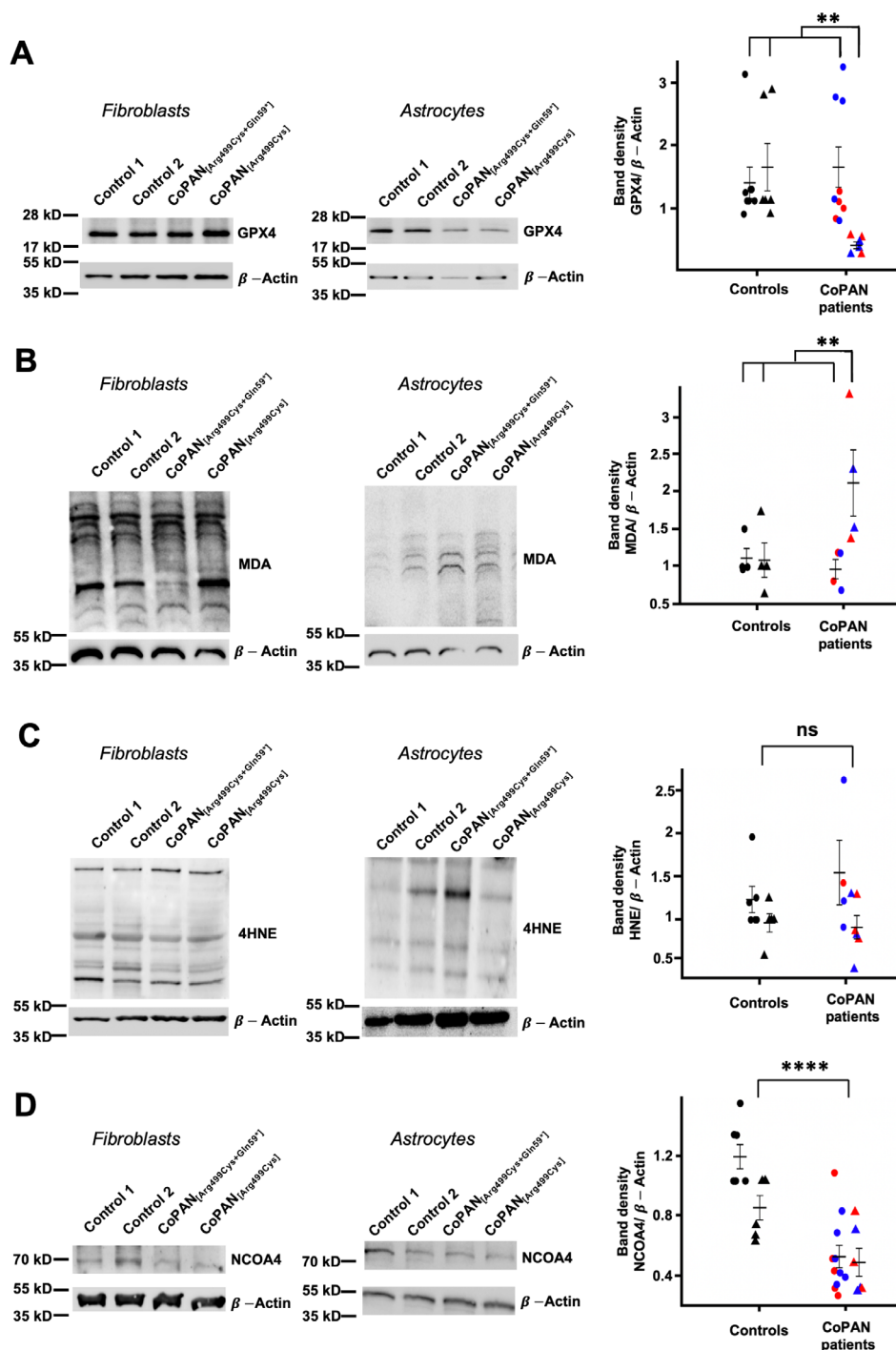


FIGURE 7 | Legend on next page.

is suggestive of a relation between CoA impairment and iron deposition.

#### 4 | Discussion

The mechanisms driving cerebral iron accumulation and its subsequent impact on various neurodegenerative diseases remain elusive. The CoPAN condition, in particular, has not been extensively studied in relation to iron overload. In this research, we employed patient-derived cellular models to delve into the

intricacies of this phenomenon and to elucidate its potential contributions to the pathogenesis of CoPAN.

The pathology is very rare and new patients have only been identified in recent years with the increasing use of exome sequencing (Cavestro et al. 2024b). We had access to the fibroblasts of the first two Italian CoPAN patients (Dusi et al. 2014), which were reprogrammed into hiPS and then derivatized to obtain d-astrocytes. We chose astrocytes because our previous studies on neuronal cell models of PKAN, another inborn error of CoA biosynthesis, have shown that these are the neuronal cells in



**FIGURE 7** | Alteration of ferroptosis in fibroblasts and d-astrocytes. Western blot analysis of soluble cell homogenates from fibroblasts (left panels) and d-astrocytes (middle panels) derived from control and CoPAN patients, differentiated for 50 days in serum B supplemented with FeAC, Apo-Tf, and Ascorbic acid. Blots were probed with the indicated antibodies and protein levels were normalized to  $\beta$ -Actin. Quantification was performed via densitometry and plotted (right panels). (A) Western blot of fibroblasts and d-astrocytes showing GPX4 expression with the relative quantification normalized to  $\beta$ -Actin. Comparison between models 1 and 2 using the Kenward-Roger test revealed a significant difference for GPX4 ( $\chi^2_1 = 5.621$ ,  $p = 0.01775$ ), leading to the selection of model 1. Analysis of Deviance indicated a significant CoPAN  $\cdot$  Cell Type interaction ( $\chi^2_1 = 7.4892$ ,  $p = 0.006207$ ). (B) Western blot of fibroblasts and d-astrocytes showing MDA expression with the relative quantification normalized to  $\beta$ -Actin. The Kenward-Roger test showed a significant difference between models 1 and 2 ( $\chi^2_1 = 7.6334$ ,  $p = 0.00573$ ), leading to the use of model 1. Analysis of Deviance indicated significant effects for CoPAN ( $\chi^2_1 = 5.9877$ ,  $p = 0.014406$ ) and the CoPAN  $\cdot$  Cell Type interaction ( $\chi^2_1 = 10.6695$ ,  $p = 0.001089$ ). (C) Western blot of fibroblasts and d-astrocytes showing 4HNE expression with the relative quantification normalized to  $\beta$ -Actin. No significant difference was found between models 1 and 2 ( $\chi^2_1 = 2.3145$ ,  $p = 0.1282$ ), and Analysis of Deviance for model 2 revealed no significant effects. (D) Western blot of fibroblasts and d-astrocytes showing NCOA4 expression with the relative quantification of NCOA4 normalized to  $\beta$ -Actin. No significant difference was observed between models 1 and 2 ( $\chi^2_1 = 3.2394$ ,  $p = 0.07189$ ), but the Analysis of Deviance indicated a significant effect of CoPAN ( $\chi^2_1 = 46.1874$ ,  $p < 0.0001$ ). Round dots indicate fibroblasts, triangular dots indicate astrocytes; black represents controls, red represents CoPAN<sub>[Arg499Cys+Gln59\*]</sub>, and blue represents CoPAN<sub>[Arg499Cys]</sub>. \*\* $p < 0.01$ , \*\*\*\* $p < 0.0001$ .

which we found the highest iron accumulation (Santambrogio et al. 2022). As we only had a limited number of patients available, we considered analyzing both cell models: fibroblasts and d-astrocytes. In contrast to PKAN fibroblasts, which did not accumulate iron, CoPAN fibroblasts indeed showed iron deposition, as did the d-astrocytes, although to different degrees between them. Specifically, we observed that iron accumulation in CoPAN fibroblasts depends on the composition of serum used in cell culture. This finding further highlights the issue that data variability in the field might depend on the use of different sources of reagents (brand, batch and lot). On the other hand, this discovery was also an important revelation, as it created a gradient of pathological phenotype related to iron accumulation. This mechanism represents a significant factor in the pathogenesis of CoPAN.

In CoPAN fibroblasts, tubulin acetylation was reduced, mitochondrial morphology indicated a non-functional organelle, and vesicular trafficking appeared to be altered, suggesting a detrimental cascade of events as in PKAN, where alteration of endocytosis reduced the ability to import iron into the mitochondrion, thus promoting cytosolic iron deposition (Santambrogio et al. 2024). From these data, we can hypothesize that the molecular mechanism of iron accumulation is very similar in the two pathologies. It is noteworthy that in both PKAN (Santambrogio et al. 2023) and CoPAN, treatment with CoA leads to a partial decline of pathogenesis. In addition, also for CoPAN, a more evident effect, compared to CoA addition, is achieved with treatment with Leriglitazone. Its proven action on mitochondrial function (Musokhranova et al. 2023) appears to be sufficient to restore correct tubulin acetylation in both patient fibroblasts.

In contrast, analysis of senescence and ferroptosis revealed differences between fibroblasts and d-astrocytes, suggesting a partially overlapping phenotype. Furthermore, data highlighted a different degree of senescence in d-astrocytes varying between the two patients, possibly due to the different gene mutations. The heterozygous CoPAN<sub>[Arg499Cys+Gln59\*]</sub> patient had a mutated dephospho-CoA kinase active site only on one allele, while both enzymatic sites were completely absent on the other. The homozygous patient had mutated dephospho-CoA kinase sites but retained 4'-phosphopantetheine adenylyl-transferase activity in both alleles. These differences could explain the varying severity

of the disease in the two patients (Dusi et al. 2014). Moreover, we hypothesize that this could also explain the different behavior in vesicular trafficking observed with Synaptozip. Nevertheless, we observed a strong correlation between the percentage of senescent cells and the percentage of cells with iron deposition. This suggests that iron accumulation and senescence occur simultaneously in both cell types, although fibroblasts appear to be more resistant to iron loading, while d-astrocytes are more susceptible to iron accumulation. Overall, the data seem to indicate that the senescence phenotype is directly related to the amount of iron. These data are supported by those previously shown in invitro models of Neuroferritinopathy, a NBIA caused by ferritin with structural defects that lost the ability to handle intracellular iron (Cozzi et al. 2021). The consequent increased cytosolic free iron induced senescence in both fibroblasts and iPS-derived neurons (Cozzi et al. 2019).

Most importantly, senescence of astrocytes that might be misinterpreted as astrocytic reactivity causes neuronal death, which could be the underlying primary cause of neurodegeneration (Cohen and Torres 2019). The relationship between iron and cellular senescence is multifaceted, with iron accumulation being a characteristic feature of senescent cells. Studies have shown that iron content increases exponentially in senescent cells, which may contribute to oxidative stress and cellular dysfunction (Killilea et al. 2003; Killilea et al. 2004). Furthermore, senescent cells exhibit alterations in iron intake and storage, and they are resistant to iron-mediated cell death pathways, such as ferroptosis, due to impaired ferritinophagy (Masaldan et al. 2018). Contradictorily, while iron accumulation is a consequence of cellular senescence, it does not appear to be a cause, as manipulating iron levels does not significantly affect the lifespan or markers of senescence in cells (Killilea et al. 2004). These previous works suggested that while iron accumulation is associated with senescence, it is not necessarily a driver of the senescence process. However, our present and previous data indicated that iron dys-homeostasis might be the principal actor in promoting senescence. This is particularly important in astrocytes where the senescent phenotype was demonstrated to be associated with neurotoxicity (Kim et al. 2024). In summary, iron accumulation is a hallmark of cellular senescence, potentially exacerbating oxidative stress and contributing to the senescent phenotype.

Also, ferroptosis affected the two cellular types differently: fibroblasts did not show convincing signs of ferroptosis, while elevated MDA and reduced GPX4 expression indicated a clearer tendency toward ferroptosis in d-astrocytes. Interestingly, primary astrocytes isolated from the brain of mice conditionally deleted for *Coasy* in the astroglial lineage were characterized by lipid peroxidation, suggesting ferroptosis (Cavestro et al. 2024a). As previously demonstrated in PKAN by d-neurons and d-astrocytes co-culture experiments, the iron-loaded cells underwent ferroptosis, promoting neurotoxicity (Santambrogio et al. 2022). Here, where the number of iron-loaded cells is higher than in PKAN, we hypothesize that astrocytes might exert the same or even more marked neuronal toxicity. Unfortunately, the CoPAN<sub>[Arg499Cys+Gln59\*]</sub> d-astrocytes, which had the highest number of iron/senescent positive cells, can only be maintained in culture for a short time after maturation, thus preventing the possibility of performing co-culture experiments. In conclusion, although this study is limited by the analysis of cells derived from only two patients, it nevertheless demonstrates a close relationship between the accumulation of cytosolic iron, caused by mitochondrial alterations, and senescence. A relationship that probably also exists in other neurodegenerations associated with mitochondrial defects and iron accumulation.

On the therapeutic side, our efforts to improve the amount of COASY by stabilizing its mRNA through the IRE/IRP system were unsuccessful. Therefore, the focus should be on attempts to improve mitochondrial health (i.e., leriglitzone treatment) and/or improve CoA supply to cells that are most affected due to defects in its biosynthesis.

#### Author Contributions

A.R. developed iPSCs, A.C. and P.S. developed the astrocyte models and maintained the iPSCs; P.S., A.C., A.P., C.B., and A.S.M. performed the in vitro analysis; C.B. and A.P. performed the biochemical analyses. S.L. and P.S. conceived the study and wrote the manuscript. V.T. and I.D.M. contributed, reviewed the manuscript, and provided comments. All authors approved the final version of the manuscript.

#### Acknowledgments

A portion of this work was carried out at ALEMBIC, which is an advanced microscopy facility. Laboratory established by the San Raffaele Scientific Institute and Vita-Salute San Raffaele University. Deferiprone was kindly provided by Dr. Fernando Tricta, ApoPharma, Toronto, Canada. Leriglitzone was kindly provided by Minoryx Therapeutics BE, A.S.M., Charleroi 6041, Belgium. Open access funding provided by BIBLIOSAN.

#### Ethics Statement

This study does not require ethical approval.

#### Conflicts of Interest

The authors declare no conflicts of interest.

#### Data Availability Statement

The datasets generated and/or analyzed during the current study are available from the corresponding authors upon reasonable request.

#### References

- Aghajanian, S., and D. M. Worrall. 2002. "Identification and Characterization of the Gene Encoding the Human Phosphopantetheine Adenyltransferase and Dephospho-CoA Kinase Bifunctional Enzyme (CoA Synthase)." *Biochemical Journal* 365, no. 1: 13–18. <https://doi.org/10.1042/bj20020569>.
- Ajit, V. K., P. Selvaraj, K. Divya, B. Thomas, R. N. Menon, and S. Sundaram. 2023. "Status Epilepticus in Coenzyme A Synthase Protein-Associated Neurodegeneration - Expanding the Clinical Phenotype." *Indian Journal of Pediatrics* 90, no. 5: 519. <https://doi.org/10.1007/s12098-023-04515-x>.
- Arber, C., P. R. Angelova, S. Wiethoff, et al. 2017. "iPSC-Derived Neuronal Models of PANK2-Associated Neurodegeneration Reveal Mitochondrial Dysfunction Contributing to Early Disease." *PLoS One* 12, no. 9: e0184104. <https://doi.org/10.1371/journal.pone.0184104>.
- Arber, C. E., A. Li, H. Houlden, and S. Wray. 2016. "Review: Insights Into Molecular Mechanisms of Disease in Neurodegeneration With Brain Iron Accumulation: Unifying Theories." *Neuropathology and Applied Neurobiology* 42, no. 3: 220–241. <https://doi.org/10.1111/nan.12242>.
- Ayala, A., M. F. Muñoz, and S. Argüelles. 2014. "Lipid Peroxidation: Production, Metabolism, and Signaling Mechanisms of Malondialdehyde and 4-Hydroxy-2-Nonenal." *Oxidative Medicine and Cellular Longevity* 2014: 1–31. <https://doi.org/10.1155/2014/360438>.
- Berti, C. C., C. Dallabona, M. Lazzaretti, et al. 2015. "Modeling Human Coenzyme A Synthase Mutation in Yeast Reveals Altered Mitochondrial Function, Lipid Content and Iron Metabolism." *Microbial Cell* 2, no. 4: 126–135. <https://doi.org/10.15698/mic2015.04.196>.
- Cavestro, C., M. D'Amato, M. N. Colombo, et al. 2024a. "CoA Synthase Plays a Critical Role in Neurodevelopment and Neurodegeneration." *Frontiers in Cellular Neuroscience* 18: 1458475. <https://doi.org/10.3389/fncel.2024.1458475>.
- Cavestro, C., F. Morra, A. Legati, et al. 2024b. "Emerging Variants, Unique Phenotypes, and Transcriptomic Signatures: An Integrated Study of COASY-Associated Diseases." *Annals of Clinical and Translational Neurology* 11, no. 6: 1615–1629. <https://doi.org/10.1002/acn3.52079>.
- Chang, C., and C. Lin. 2011. "Eye-Of-The-Tiger Sign Is Not Pathognomonic of Pantothenate Kinase-Associated Neurodegeneration in Adult Cases." *Brain and Behavior* 1, no. 1: 55–56. <https://doi.org/10.1002/brb3.8>.
- Cohen, J., and C. Torres. 2019. "Astrocyte Senescence: Evidence and Significance." *Aging Cell* 18, no. 3: 1–14. <https://doi.org/10.1111/accel.12937>.
- Cozzi, A., S. Levi, E. Bazzigaluppi, G. Ruggeri, and P. Arosio. 1989. "Development of an Immunoassay for all Human Isoferritins, and Its Application to Serum Ferritin Evaluation." *Clinica Chimica Acta* 184, no. 3: 197–206. [https://doi.org/10.1016/0009-8981\(89\)90052-1](https://doi.org/10.1016/0009-8981(89)90052-1).
- Cozzi, A., D. I. Orellana, P. Santambrogio, et al. 2019. "Stem Cell Modeling of Neuroferritinopathy Reveals Iron as a Determinant of Senescence and Ferroptosis During Neuronal Aging." *Stem Cell Reports* 13, no. 5: 832–846. <https://doi.org/10.1016/j.stemcr.2019.09.002>.
- Cozzi, A., P. Santambrogio, M. Ripamonti, E. Rovida, and S. Levi. 2021. "Pathogenic Mechanism and Modeling of Neuroferritinopathy." *Cellular and Molecular Life Sciences* 78, no. 7: 3355–3367. <https://doi.org/10.1007/s00018-020-03747-w>.
- Doll, S., and M. Conrad. 2017. "Iron and Ferroptosis: A Still Ill-Defined Liaison." *IUBMB Life* 69, no. 6: 423–434. <https://doi.org/10.1002/iub.1616>.
- Dusi, S., L. Valletta, T. B. Haack, et al. 2014. "Exome Sequence Reveals Mutations in CoA Synthase as a Cause of Neurodegeneration With Brain Iron Accumulation." *American Journal of Human Genetics* 94, no. 1: 11–22. <https://doi.org/10.1016/j.ajhg.2013.11.008>.

- Evers, C., A. Seitz, B. Assmann, et al. 2017. "Diagnosis of CoPAN by Whole Exome Sequencing: Waking Up a Sleeping Tiger's Eye." *American Journal of Medical Genetics, Part A* 173, no. 7: 1878–1886. <https://doi.org/10.1002/ajmg.a.38252>.
- Ferro, M., J. Lamanna, M. Ripamonti, et al. 2017. "Functional Mapping of Brain Synapses by the Enriching Activity-Marker SynaptoZip." *Nature Communications* 8, no. 1: 1229. <https://doi.org/10.1038/s41467-017-01335-4>.
- Galdieri, L., T. Zhang, D. Rogerson, R. Lleshi, and A. Vancura. 2014. "Protein Acetylation and Acetyl Coenzyme a Metabolism in Budding Yeast." *Eukaryotic Cell* 13, no. 12: 1472–1483. <https://doi.org/10.1128/EC.00189-14>.
- Hashemi, N., R. Nejad Shahrokh Abadi, A. Alavi, A. R. Tavasoli, and M. Rohani. 2023. "A Mild Form of Neurodegeneration With Brain Iron Accumulation Attributed to Coenzyme A Synthase Mutation." *Movement Disorders Clinical Practice* 10, no. 2: 331–334. <https://doi.org/10.1002/mdc3.13624>.
- Hayflick, S. J. 2023. "A Brief History of NBIA Gene Discovery." *Journal of Movement Disorders* 16, no. 2: 133–137. <https://doi.org/10.14802/jmd.23014>.
- Hentze, M. W., M. U. Muckenthaler, B. Galy, and C. Camaschella. 2010. "Two to Tango: Regulation of Mammalian Iron Metabolism." *Cell* 142, no. 1: 24–38. <https://doi.org/10.1016/j.cell.2010.06.028>.
- Khatrri, D., D. Zizioli, N. Tiso, et al. 2016. "Down-Regulation of Coasy, the Gene Associated With NBIA-VI, Reduces Bmp Signaling, Perturbs Dorsal-Ventral Patterning and Alters Neuronal Development in Zebrafish." *Scientific Reports* 6: 1–15. <https://doi.org/10.1038/srep37660>.
- Killilea, D. W., H. Atamna, C. Liao, and B. N. Ames. 2003. "Iron Accumulation During Cellular Senescence in Human Fibroblasts In Vitro." *Antioxidants and Redox Signaling* 5, no. 5: 507–516. <https://doi.org/10.1089/152308603770310158>.
- Killilea, D. W., S. L. Wong, H. S. Cahaya, H. Atamna, and B. N. Ames. 2004. "Iron Accumulation During Cellular Senescence." *Annals of the New York Academy of Sciences* 1019, no. 1: 365–367. <https://doi.org/10.1196/annals.1297063>.
- Kim, J., I. D. Yoo, J. Lim, and J. S. Moon. 2024. "Pathological Phenotypes of Astrocytes in Alzheimer's Disease." *Experimental and Molecular Medicine* 56, no. 1: 95–99. <https://doi.org/10.1038/s12276-023-01148-0>.
- Kruer, M. C., M. Hiken, A. Gregory, et al. 2011. "Novel Histopathologic Findings in Molecularly-Confirmed Pantothenate Kinase-Associated Neurodegeneration." *Brain* 134, no. 4: 947–958. <https://doi.org/10.1093/brain/awr042>.
- Le, Y., Q. Liu, Y. Yang, and J. Wu. 2024. "The Emerging Role of Nuclear Receptor Coactivator 4 in Health and Disease: A Novel Bridge Between Iron Metabolism and Immunity." *Cell Death Discovery* 10, no. 1: 1–13. <https://doi.org/10.1038/s41420-024-02075-3>.
- Leonardi, R., Y. Zhang, C. Rock, and S. Jackowski. 2005. "Coenzyme A: Back in Action." *Progress in Lipid Research* 44, no. 2–3: 125–153. <https://doi.org/10.1016/j.plipres.2005.04.001>.
- Lin, C. C., M. Kitagawa, X. Tang, et al. 2018. "CoA Synthase Regulates Mitotic Fidelity via CBP-Mediated Acetylation." *Nature Communications* 9, no. 1: 1039. <https://doi.org/10.1038/s41467-018-03422-6>.
- Mahale, R. R., R. Singh, P. Katragadda, and H. Padmanabha. 2023. "COASY Protein-Associated Neurodegeneration: Report From India." *Annals of Indian Academy of Neurology* 26, no. 5: 834–836. [https://doi.org/10.4103/aian.aian\\_456\\_23](https://doi.org/10.4103/aian.aian_456_23).
- Malatesta, M., M. Giagnacovo, L. V. Renna, R. Cardani, G. Meola, and C. Pellicciari. 2011. "Cultured Myoblasts From Patients Affected by Myotonic Dystrophy Type 2 Exhibit Senescence-Related Features: Ultrastructural Evidence." *European Journal of Histochemistry: EJH* 55, no. 3: e26. <https://doi.org/10.4081/ejh.2011.e26>.
- Masaldan, S., S. A. S. Clatworthy, C. Gamell, et al. 2018. "Iron Accumulation in Senescent Cells Is Coupled With Impaired Ferritinophagy and Inhibition of Ferroptosis." *Redox Biology* 14: 100–115. <https://doi.org/10.1016/j.redox.2017.08.015>.
- Di Meo, I., C. Cavestro, S. Pedretti, et al. 2020. "Neuronal Ablation of Coa Synthase Causes Motor Deficits, Iron Dyshomeostasis, and Mitochondrial Dysfunctions in a Copan Mouse Model." *International Journal of Molecular Sciences* 21, no. 24: 1–20. <https://doi.org/10.3390/ijms21249707>.
- Mishra, R., S. Kulshreshtha, K. Mandal, et al. 2022. "COASY Related Pontocerebellar Hypoplasia Type 12: A Common Indian Mutation With Expansion of the Phenotypic Spectrum." *American Journal of Medical Genetics Part A* 188, no. 8: 2339–2350. <https://doi.org/10.1002/ajmg.a.62768>.
- Musokhranova, U., C. Grau, C. Vergara, et al. 2023. "Mitochondrial Modulation With Leriglitazone as a Potential Treatment for Rett Syndrome." *Journal of Translational Medicine* 21, no. 1: 1–17. <https://doi.org/10.1186/s12967-023-04622-5>.
- Orellana, D. I., P. Santambrogio, A. Rubio, et al. 2016. "Coenzyme A Corrects Pathological Defects in Human Neurons of PANK 2-Associated Neurodegeneration." *EMBO Molecular Medicine* 8, no. 10: 1197–1211. <https://doi.org/10.15252/emmm.201606391>.
- Ripamonti, M., P. Santambrogio, G. Racchetti, et al. 2022. "PKAN hiPS-Derived Astrocytes Show Impairment of Endosomal Trafficking: A Potential Mechanism Underlying Iron Accumulation." *Frontiers in Cellular Neuroscience* 16: 878103. <https://doi.org/10.3389/fncel.2022.878103>.
- Rosati, J., J. Johnson, Z. Stander, et al. 2023. "Progressive Brain Atrophy and Severe Neurodevelopmental Phenotype in Siblings With Biallelic COASY Variants." *American Journal of Medical Genetics Part A* 191, no. 3: 842–845. <https://doi.org/10.1002/ajmg.a.63076>.
- Santambrogio, P., A. Cozzi, C. Balestrucci, and M. Ripamonti. 2024. "Mitochondrial Iron de Fe Cieny Triggers Cytosolic Iron Overload in PKAN hiPS-Derived Astrocytes." *Cell Death & Disease* 15, no. 5: 361. <https://doi.org/10.1038/s41419-024-06757-9>.
- Santambrogio, P., A. Cozzi, I. Di Meo, et al. 2023. "PPAR Gamma Agonist Leriglitazone Recovers Alterations due to Pank2-Deficiency in hiPS-Derived Astrocytes." *Pharmaceutics* 15, no. 1: 1–14. <https://doi.org/10.3390/pharmaceutics15010202>.
- Santambrogio, P., M. Ripamonti, A. Cozzi, et al. 2022. "Massive Iron Accumulation in PKAN-Derived Neurons and Astrocytes: Light on the Human Pathological Phenotype." *Cell Death and Disease* 13, no. 2: 185. <https://doi.org/10.1038/s41419-022-04626-x>.
- Santambrogio, P., M. Ripamonti, C. Paolizzi, et al. 2020. "Harmful Iron-Calcium Relationship in Pantothenate Kinase Associated Neurodegeneration." *International Journal of Molecular Sciences* 21, no. 10: 1–18. <https://doi.org/10.3390/ijms21103664>.
- Siudeja, K., B. Srinivasan, L. Xu, et al. 2011. "Impaired Coenzyme A Metabolism Affects Histone and Tubulin Acetylation in Drosophila and Human Cell Models of Pantothenate Kinase Associated Neurodegeneration." *EMBO Molecular Medicine* 3, no. 12: 755–766. <https://doi.org/10.1002/EMMM.201100180>.
- Takahashi, K., and S. Yamanaka. 2006. "Induction of Pluripotent Stem Cells From Mouse Embryonic and Adult Fibroblast Cultures by Defined Factors." *Cell* 126, no. 4: 663–676. <https://doi.org/10.1016/j.cell.2006.07.024>.
- Ursini, F., and M. Maiorino. 2020. "Lipid Peroxidation and Ferroptosis: The Role of GSH and GPx4." *Free Radical Biology and Medicine* 152: 175–185. <https://doi.org/10.1016/j.freeradbiomed.2020.02.027>.
- van Dijk, T., S. Ferdinandusse, J. P. N. Ruiter, et al. 2018. "Biallelic Loss of Function Variants in COASY Cause Prenatal Onset Pontocerebellar Hypoplasia, Microcephaly, and Arthrogryposis." *European Journal of Human Genetics* 26, no. 12: 1752–1758. <https://doi.org/10.1038/s41431-018-0233-0>.

Zheng, Y., T. Liufu, B. Wen, et al. 2024. "COASY Variant as a New Genetic Cause of Riboflavin-Responsive Lipid Storage Myopathy." *Cell Discovery* 10, no. 1: 23–26. <https://doi.org/10.1038/s41421-023-00641-0>.

### **Supporting Information**

Additional supporting information can be found online in the Supporting Information section.